Article

A Positron Emission Tomography Tracer Targeting the S2 Subunit of SARS-CoV-2 in Extrapulmonary Infections

Jianzhong Xian,[||] Hongbin Huang,[||] Guolong Huang, Renwei Zhou, Min Yang, Yifan Qiu, Lei Bi, Zhongzhen Su, Fei Xiao, Hong Shan,* and Hongjun Jin*

Cite This: https://doi.org/10.1021/acs.molpharmaceut.2c00584

Read Online

ACCESS | Metrics & More | Article Recommendations | Supporting Information

ABSTRACT: Tracking the pathogen of coronavirus disease 2019 (COVID-19) in live subjects may help estimate the spatiotemporal distribution of SARS-CoV-2 infection *in vivo*. This study developed a positron emission tomography (PET) tracer of the S2 subunit of spike (S) protein for imaging SARS-CoV-2. A pan-coronavirus inhibitor, EK1 peptide, was synthesized and radiolabeled with copper-64 after being conjugated with 1,4,7-triazacyclononane-1,4,7-triyl-triacetic acid (NOTA). The *in vitro* stability tests indicated that $[^{64}Cu]$Cu-NOTA-EK1 was stable up to 24 h both in saline and in human serum. The binding assay showed that $[^{64}Cu]$Cu-NOTA-EK1 has a nanomolar affinity (K_i = 3.94 ± 0.51 nM) with the S-protein of SARS-CoV-2. The cell uptake evaluation used HEK293T/S+ and HEK293T/S− cell lines that showed that the tracer has a high affinity with the S-protein on the cellular level. For the *in vivo* study, we tested $[^{64}Cu]$Cu-NOTA-EK1 in HEK293T/S+ cell xenograft-bearing mice (n = 3) and pseudovirus of SARS-CoV-2-infected HEK293T/ACE2 cell bearing mice (n = 3). The best radioactive xenograft-to-muscle ratio ($X/N^{xenograft}$ 8.04 ± 0.99, $X/N^{pseudovirus}$ 6.47 ± 0.71) was most evident 4 h postinjection. Finally, PET imaging in the surrogate mouse model of beta-coronavirus, mouse hepatic virus-A59 infection in C57BL/6 J mice showed significantly enhanced accumulation in the liver than in the uninfected mice (1.626 ± 0.136 vs 0.871 ± 0.086 %ID/g, n = 3, P < 0.05) at 4 h postinjection. In conclusion, our experimental results demonstrate that $[^{64}Cu]$Cu-NOTA-EK1 is a potential molecular imaging probe for tracking SARS-CoV-2 in extrapulmonary infections in living subjects.

KEYWORDS: molecular imaging, S2 subunit of SARS-CoV-2, EK1 peptide, positron emission tomography (PET)
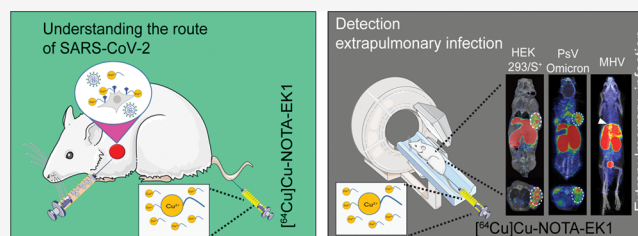
1. INTRODUCTION

Since the outbreak of the coronavirus disease 2019 (COVID-19), evolution and mutations in severe acute respiratory syndrome coronavirus 2 (SARS-CoV-2) have resulted in the generation of virulent, highly contagious mutant strains, such as the Delta (B.1.617.2) and Omicron (B.1.1.529) variants.[1,2] Reports regarding extrapulmonary infection and symptoms associated with SARS-CoV-2 disorders, including the digestive tract,[3] heart,[4] kidneys,[5] eyes,[6] liver,[7] and even the brain,[8] are increasing. Adverse symptoms and extrapulmonary lesions continue to bother recovering patients for an extended period.[9] The presence of SARS-CoV-2 RNA as detected by a reverse-transcription polymerase chain reaction (RT-PCR) test equates to a definitive diagnosis of COVID-19.[10] However, detecting the presence of extrapulmonary viruses is not an easy task. Traditional imaging methods, including CT, MRI, and ultrasound, can show anatomical information but do not directly detect the presence of the virus.[11-13]

Molecular imaging is noninvasive, functional, and considered a clinical cornerstone for detecting virion with specific molecular events.[14,15] Positron emission tomography (PET) has emerged as a noninvasive and sensitive molecular imaging technology based on molecules with excellent sensitivity that provides functional clues about insignificant changes in accompanying biomarkers of diseases.[15] 18F-FDG PET/CT has been used to monitor disease progression in COVID-19 patients.[16,17] Although 18F-FDG is widely used, it does not precisely target viral infections. Zhu et al. reported a PET agent targeting angiotensin-converting enzyme 2 (ACE2) for non-invasively investigating organs impaired by COVID-19.[18] Ruiz-Bedoya et al. developed a probe that activates alveolar inflammatory macrophages to monitor lung damage.[19] However, there is no effective tracer directly targeting SARS-CoV-2 for monitoring current and emerging virus strains in living subjects.

The coronavirus needs to fuse its lipid envelope with the host cell membrane before it can enter host cells. The spike (S) glycoprotein is essential for activating virus-mediated cell entry and membrane fusion[20,21] and has long been considered
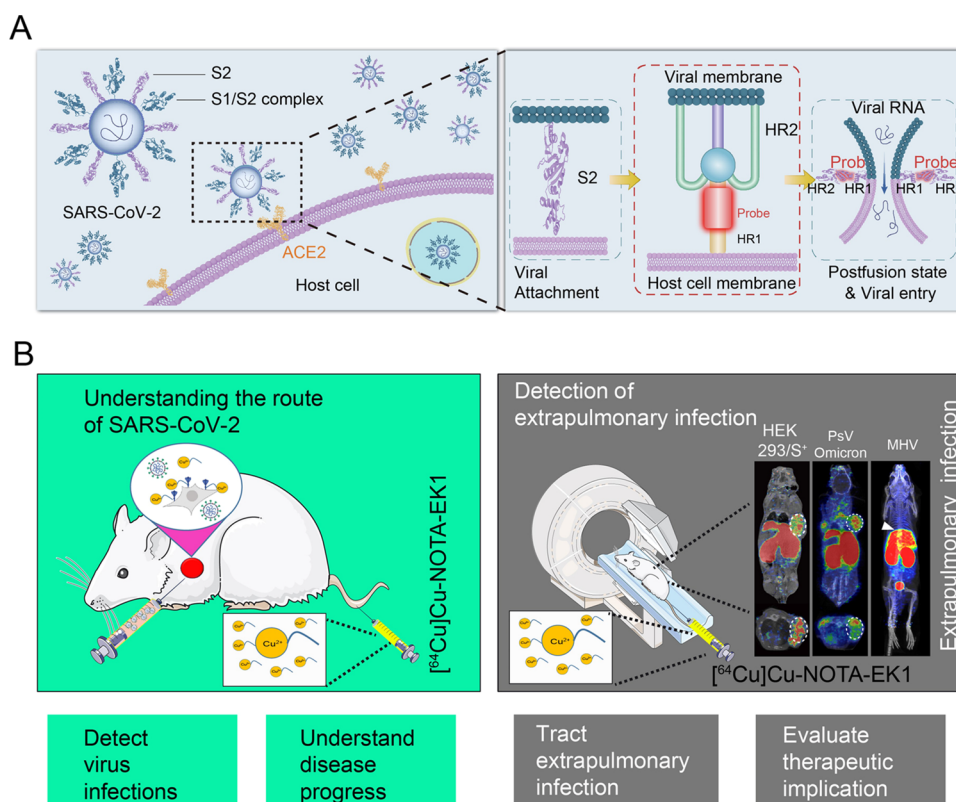
Figure 1. Schematic illustration of the EK1 peptide probe targeting SARS-CoV-2 infections in live subjects. (A) SARS-CoV-2 uses spike (S) protein to invade host cells, including anchor ACE2 (with S1 subunit) and membrane fusion (with S2 subunit). Compared to the mutable S1 subunit, the S2 subunit is very conservative. Also, the probes that target the heptad repeat 1 (HR1) domain of the S2 subunit are more effective. (B) To accurately mimic the disease process of COVID-19 in the BSL-2 environment, we generated a HEK293T/ACE2 cells xenograft-bearing mice model infected with the SARS-CoV-2 pseudovirus to evaluate the imaging probes for tracking the S-protein. The probe's effectiveness for detecting extrapulmonary infection was also tested in mouse hepatic virus 59 (MHV-A59) infected C57BL/6 mice using PET/CT imaging.

one of the targets in virus treatment, prevention, and control.[22,23] The S1 and S2 subunits of the S-protein play different roles in the invasion of human cells. The S1 subunit is responsible for finding and anchoring cells expressing ACE2 receptors.[24] After the receptor-binding domain (RBD) of the S1 subunit binds to ACE2 receptors in human cells, the S2 subunit undergoes a conformational change. First, the fusion peptide is exposed and inserted into the cellular membrane. Then, three domains of heptad repeats (HR) merge to form the internal trimer of a six-helix bundle (6-HB) with exposed hydrophobic grooves. These grooves promote viral infection of human cells (Figure 1A). Therefore, the 6-HB of the S2 subunit mediating membrane fusion is a critical structure for an active infectious virus.

Molecular imaging agents that target the S2 subunit of SARS-CoV-2, which is more conserved than the RBD of the S1 subunit, may be more effective and efficient in detecting SARS-CoV-2 variants of concern (VOC). Cai et al. reported that both the prefusion spikes (with the S1 subunit) and the postfusion spikes (without the S1 subunit) were present on the surface of mature virions, and the proportion of prefusion and postfusion spikes varied depending on the status of virion maturation.[25] This study suggested that the intermediate state of the S2 subunit can be tracked in the live virions (Figure 1B). Furthermore, studies regarding cell fusion mechanisms found that the EK1 peptide derived from the HR2 domain of the S2 subunit of SARS-CoV, and its binding site is compatible with that of natural HR2, forming a similar 6-HB structure.[26] The

EK1 sequence matched reasonably well with the HR2 domain of all those virus strains: SARS-CoV, SARS-CoV-2, and the mouse beta-coronavirus, mouse hepatic virus (MHV)-A59. This study used the radiotracer [⁶⁴Cu]Cu-NOTA-EK1 for PET imaging. This tracer has the potential to quantify the SARS-CoV-2 distribution in live subjects and to evaluate therapeutic intervention of SARS-CoV-2 in animal models.

2. MATERIALS AND METHODS

2.1. Synthesis of [⁶⁴Cu]Cu-NOTA-EK1. The amino acid sequence of EK1 was SLDQINVTFLDLEYEMKKLEEAIKKL-EESYIDLKEL according to the literature.[27] We synthesized it using the N-terminus labeled with a chelating agent, 1,4,7-triazacyclononane-1,4,7-triyl-triacetic acid (NOTA), to form the precursor NOTA-EK1 (Figure S1). Next, precursor NOTA-EK1 was radiolabeled with copper-64. Radioisotope [⁶⁴Cu]CuCl₂ was purchased from Atomic High Tech Radiopharmaceutical Co., Ltd. (Beijing, China) with up to 98% radio-nuclidic purity. NOTA-EK1 (100 μg) was dissolved in 50 μL of NaAc buffer (0.5 M, pH 5.0), thoroughly combined via pipette mixing, added with [⁶⁴Cu]CuCl₂ (100 μL, ∼300 MBq, pH 5.0), mixed thoroughly, and incubated at room temperature for 15 min. Radioactive thin layer chromatography (radio-TLC) was used to monitor the radiochemical conversion (RCC) at 2, 5, 10, and 15 min. When the RCC was greater than 99%, the mixture was diluted and loaded onto a Sep-Pak C18 light cartridge (Waters Inc., Milford, USA). [⁶⁴Cu]Cu-NOTA-EK1 was eluted and dried under a gentle

stream of nitrogen. Next, the concentrate was diluted with a sterile saline solution. Radioactive high-performance liquid chromatography (radio-HPLC) was used to perform the quality control.

2.2. Stability Studies of [^{64}Cu]Cu-NOTA-EK1. *In vitro* stability of [^{64}Cu]Cu-NOTA-EK1 was evaluated in human serum and normal saline. [^{64}Cu]Cu-NOTA-EK1 (2.05–3.50 MBq) was mixed with 0.5 mL of human serum or normal saline at 37 °C independently for 2, 12, and 24 h. [^{64}Cu]Cu-NOTA-EK1 was then tested using radio-HPLC as previously described.[28]

2.3. *In Vitro* Binding Studies. We performed binding experiments to verify the binding potency of the tracer. The recombinant S-protein of SARS-CoV-2 (10 ng/well) was immobilized in a 96-well plate (Corning Costar, New York, USA) at 4 °C overnight. Then, 3% bovine serum albumin (BSA) in phosphate buffered saline (PBS) (pH 7.4) was used to block the wells for 1 h, and serial dilutions (500.0, 166.7, 55.6, 18.5, 6.2, 2.1, 0.7, and 0.2 nM) of biotin-EK1 were added to the plate for 1 h at 37 °C. Next, the plate was washed with PBS three times to remove the unbound peptide. The bound peptide was detected using streptavidin-HRP for 1 h at room temperature. TMB (CXWBiotech, Beijing, China) was applied as a substrate. A microplate reader (Synergy HTX, BioTek Inc., Lexington, USA) was used to test the absorbance at 450 nm. The saturation binding data were curve-fitted to a saturation binding model to acquire the dissociation constant (K_d). Likewise, the competitive binding assay was carried out by continuous incubation of biotin-EK1 (10 nM) with serial dilutions (500.0, 166.7, 55.6, 18.5, 6.2, 2.1, 0.7, and 0.2 nM) of NOTA-EK1 using the same procedure mentioned above. The competitive binding result of NOTA-EK1 was curve-fitted to a three-parameter competitive binding model using GraphPad Prism 8.0 to derive the half-maximal inhibitory concentration (IC_{50}). The inhibition constant (K_i) of NOTA-EK1 was calculated from the IC_{50} according to the Cheng–Prusoff equation: $K_i = IC_{50}/(1 + [\text{bioin-EK1}]/K_d)$.

We performed cell uptake analysis to test the binding capability of [^{64}Cu]Cu-NOTA-EK1 with HEK293T/S$^+$ cells. First, the HEK293T/S$^+$ and HEK293T/S$^-$ cell suspension was evenly spread into a 12-well plate (1×10^4 cells/well), shaken until the cells were evenly dispersed, and incubated in a constant-temperature cell incubator. Then, [^{64}Cu]Cu-NOTA-EK1 (0.185 MBq) (serum-free DMEM dilution) was added to each well and incubated at 37 °C for 2 and 4 h. Next, the supernatant was carefully removed, and the cells were washed 3 times with 0.01 M PBS (pH 7.4) by applying the vacuum aspiration. Finally, cells bound with the radioactive probe were collected into gamma counter test tubes and analyzed with a fully automated gamma counter (WIZARD, PerkinElmer Inc., Waltham, USA).

2.4. Plasmids and Cell Lines. The nucleotide sequences encoding human ACE2 (hACE2, accession ID: AB046569.1) were synthesized and cloned into PCDH-MCS-CMV-EF1α-puro. Plasmids encoding the Omicron variant (B.1.1.529) (Cat: plv-spike-v11) of SARS-CoV-2 S glycoprotein were purchased from InvivoGen. In addition, the coding sequences of HR1-L6-HR2 of SARS-CoV-2 (HR1: residues 910–988, HR2: residues 1162–1206, and Linker: SGGRGG) were synthesized as previously described[22] and subcloned into the lentiviral backbone plasmid encoding a reporter luciferase protein, pCDH-CMV-MCS-EF1-luciferase-puro, between the EcoR I and Not I sites. We obtained pCDH-S-puro plasmids

by subcloning the full-length gene encoding the SARS-CoV-2S-protein (Met1-Thr1273, accession ID: QHD43416.1) into the vector pCDH-CMV-MCS-EF1-PuroPCDH at the EcoRI and Not I site.

The HEK293T cell line stably expressing the SARS-CoV-2S-protein or hACE2 was successfully established after vector transfection, followed by selection with 20 μg/mL of puromycin (Solarbio, Beijing, China) (Figure S3A, B). HEK293T, HEK293T-Spike (HEK293T/S$^+$), and HEK293T/ACE2 cell lines were cultivated in Dulbecco's modified Eagle's Medium (DMEM) containing 10% fetal bovine serum, penicillin (100 U/mL), and streptomycin (100 μg/mL). In addition, HEK293T/S$^+$ and HEK293T/ACE2 cells were grown in the same medium supplemented with puromycin (20 μg/mL) at 37 °C in a humidified atmosphere with 5% CO$_2$.

2.5. SARS-CoV-2 Spike Protein Pseudotyping Lentiviral Particles. Using a lentivirus packaging system, we constructed a SARS-CoV-2 spike pseudovirus (PsV). HEK293T cells were cotransfected with a packaging plasmid pspax2, a lentivirus vector expressing luciferase (pCDH-S2-Luc-puro) or GFP (pSin-GFP), a spike pseudotyping plasmid with the Omicron variant (B.1.1.529) (Figure S3). At 48 and 72 h post-transfection, the supernatants were harvested, passed through a 0.45 μm filter, and pelleted at 2000 g for 5 min. The lentivirus was concentrated by polyethylene glycol 8000 (PEG 8000) precipitation, and its titer was measured using the Lenti-X p24 Rapid Titer Kit (Takara Bio USA Inc., Kyoto, Japan).

2.6. Immunofluorescence Assay. Immunofluorescence (IF) staining was performed to confirm that HEK293T/S$^+$ cells expressed the S-protein of SARS-CoV-2. Confluent cells (20,000 to 30,000/well) were seeded in eight-chambered glass slides the day before the *in vitro* experiments. After culturing for 24 h, cells were fixed with 4% paraformaldehyde and blocked with 3% bovine serum albumin (BSA) in PBS. Afterward, an anti-S-protein antibody (Monoclonal Rabbit IgG Clone #0004, Cat: 40592-R0004, SinoBiological, Beijing, China) was added and incubated at 4 °C overnight. After washing cells with cold PBS, a secondary antibody was added and incubated for 1 h. Then the cells were washed and counterstained with DAPI, and later examined using a confocal microscope (Zeiss880, Carl Zeiss AG Inc., Oberkochen, Germany).

2.7. Animal Experiments. All experimental rodents were maintained under pathogen-free conditions and conducted with the approval and under the supervision of the Institutional Animal Care and Use Committee (IACUC) at the Guangdong Provincial Engineering Research Center of Molecular Imaging, Guangdong Provincial Key Laboratory of Biomedical Imaging in the Fifth Affiliated Hospital of Sun Yat-sen University. All animal procedures were carried out following the Ethical Guidelines for Animal Experiments of the Fifth Affiliated Hospital, Sun Yat-sen University (protocol #00065). Male severe combined immunodeficiency (SCID) mice, male BALB/c nude mice, and male C57BL/6 J mice, ranging in age from 4 to 6 weeks, were purchased from the Guangdong Medical Laboratory Animal Center (Guangzhou, China). HEK293T/S$^+$ cells, HEK293T/S$^-$ cells, and HEK293T/ACE2 cells (all were about 5.0×10^6) in 100 μL of a 1:1 mixture of Matrigel and PBS were implanted into the right shoulder flank. The xenografts were approved to develop for about 10–14 days until they reached about 10 mm in diameter. For PsV infection, HEK293T/ACE2 xenograft-
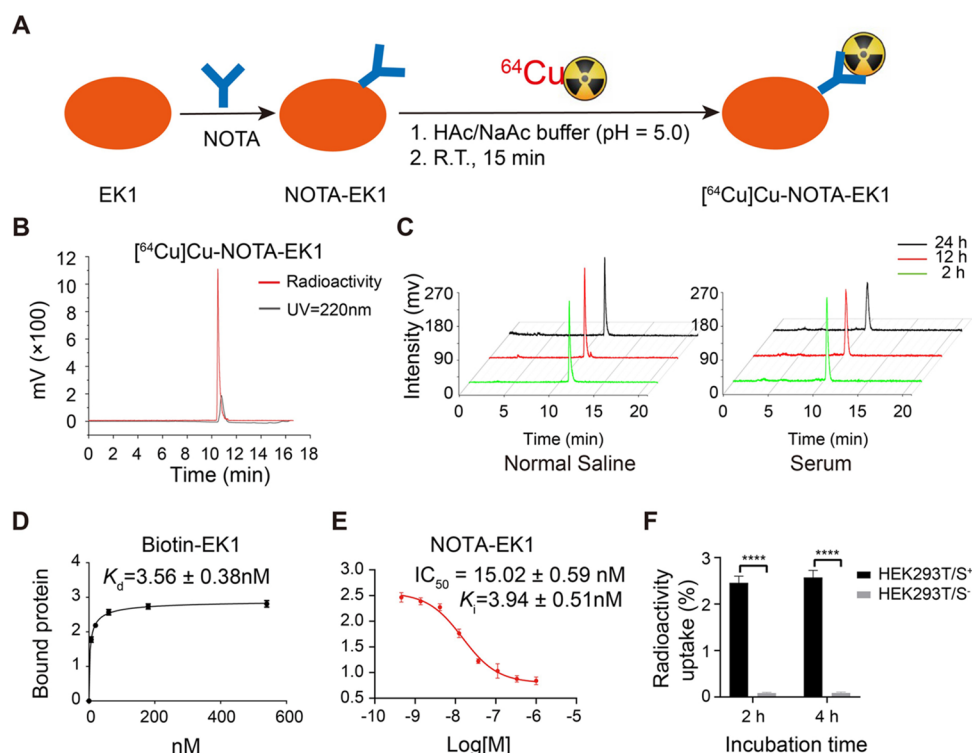
Figure 2. Preparation and characterization of [^{64}Cu]Cu-NOTA-EK1. (A) Diagram of the radiosynthesis procedure of [^{64}Cu]-NOTA-EK1 by [^{64}Cu]CuCl$_2$ and precursor NOTA-EK1. (B) Radio-HPLC profiles for final purified [^{64}Cu]Cu-NOTA-EK1 (molar activity: 10.5–15.0 GBq/μmol). (C) Stability of [^{64}Cu]Cu-NOTA-EK1 was measured by radio-HPLC after incubation in saline and human serum for up to 24 h. (D) Saturation binding experiments tested the binding dissociated constant (K_d) of Biotin-EK1 to S-protein of SARS-CoV-2. (E) IC50 values of NOTA-EK1 binding to S-protein of SARS-CoV-2 were tested in a competitive binding assay, indicating that NOTA-EK1 bind to the S-protein of SARS-CoV-2 with nanomolar affinity. (F) Cell uptake of [^{64}Cu]Cu-NOTA-EK1 in 293 T/S$^+$ and HEK293 T/S$^-$ cell lines. Data are presented as means ± SD, $n = 4$.

bearing BALB/c nude mice were injected intratumorally with 1.0×10^8 infectious units (IFU) of pseudotyped viruses covered with the S-protein of the latest SARS-CoV-2 Omicron variant. Three days after PsV infection, the count of infectious cells in HEK293T/ACE2 xenografts was measured using IVIS (PerkinElmer Inc., USA) to catch bioluminescence imaging. For PET/CT (Mediso Inc., Budapest, Hungary) imaging, HEK293T/ACE2 xenografts' signal was detected three days postinfection with lentiviral particles pseudotyped from the spike protein of the Omicron variant. To establish a surrogate mouse model of COVID-19, C57BL/6 J mice were under isoflurane-induced anesthesia and then inoculated intranasally with 30 μL of MHV-A59 at a 5×10^5 plaque-forming unit (PFU).[29] Meanwhile, the control mice were inoculated with 30 μL of PBS. Five days postinfection, PET/CT imaging and *ex vivo* biodistribution of MHV-A59-infected mice were performed.

2.8. Cytotoxicity and *In Vivo* Toxicity Assessment. Cell viability was measured using IncuCyte S3 (ESSEN Bioscience Inc., Michigan City, USA). Briefly, 50,000 HEK293T cells were plated into 6-wells, treated with 1000 μM NOTA-EK1, and allowed to attach and grow for 48 h. Acute toxicity was tested using an *in vivo* model by injection of NOTA-EK1 (50 mg/kg) and normal saline into two groups of C57BL/6 J mice ($n = 5$). In addition, the weights of the mice were observed every two days for up to two weeks (Figure S4). Furthermore, the mice were subjected to echocardiography via the Vevo LAZR-X Imaging System (Fujifilm Visual Sonics,

Toronto, Canada) on day 14. Finally, the mice were sacrificed for histopathological evaluation.

2.9. PET/CT Imaging and *Ex Vivo* Biodistribution. PET/CT imaging of the HEK293T/S$^+$, HEK293T/S$^-$ xenograft-bearing mice model, and HEK293T/ACE2 xenograft-bearing mice infected with PsV was performed 10–14 days after xenograft inoculation. Each mouse was administered ~9.25 MBq of [^{64}Cu]Cu-NOTA-EK1 through the tail vein. PET/CT images were acquired at 1, 4, 8, 12, and 24 h after injection using a small animal nano PET/CT system while the mice were under 1–2% isoflurane-induced anesthesia. Images were analyzed with Carimas software (Turku PET Centre, Helsinki, Finland). For the *in vivo* mouse model of MHV-A59-infected, PET/CT imaging was performed five days after inoculating intranasally with MHV-A59. The maximum standardized uptake values (SUV) were calculated according to the radioactivity concentration in the volume of interest, the injected dose, and the weight of the mice. The *ex vivo* biodistribution studies of the probe [^{64}Cu]Cu-NOTA-EK1 were performed by euthanizing mice 24 h postinjection. First, the major organs and xenografts were harvested and weighed. The radioactivity in each specimen was then measured using a γ-counter.

2.10. Immunohistochemistry and Immunofluorescence Staining. Immunohistochemistry (IHC) and IF staining were performed to verify the expression of the S-protein in xenograft tissue. Excised xenografts were fixed in 10% buffered formalin, embedded in paraffin, and sectioned at 4 μm thickness. Hematoxylin–eosin (H&E) staining was
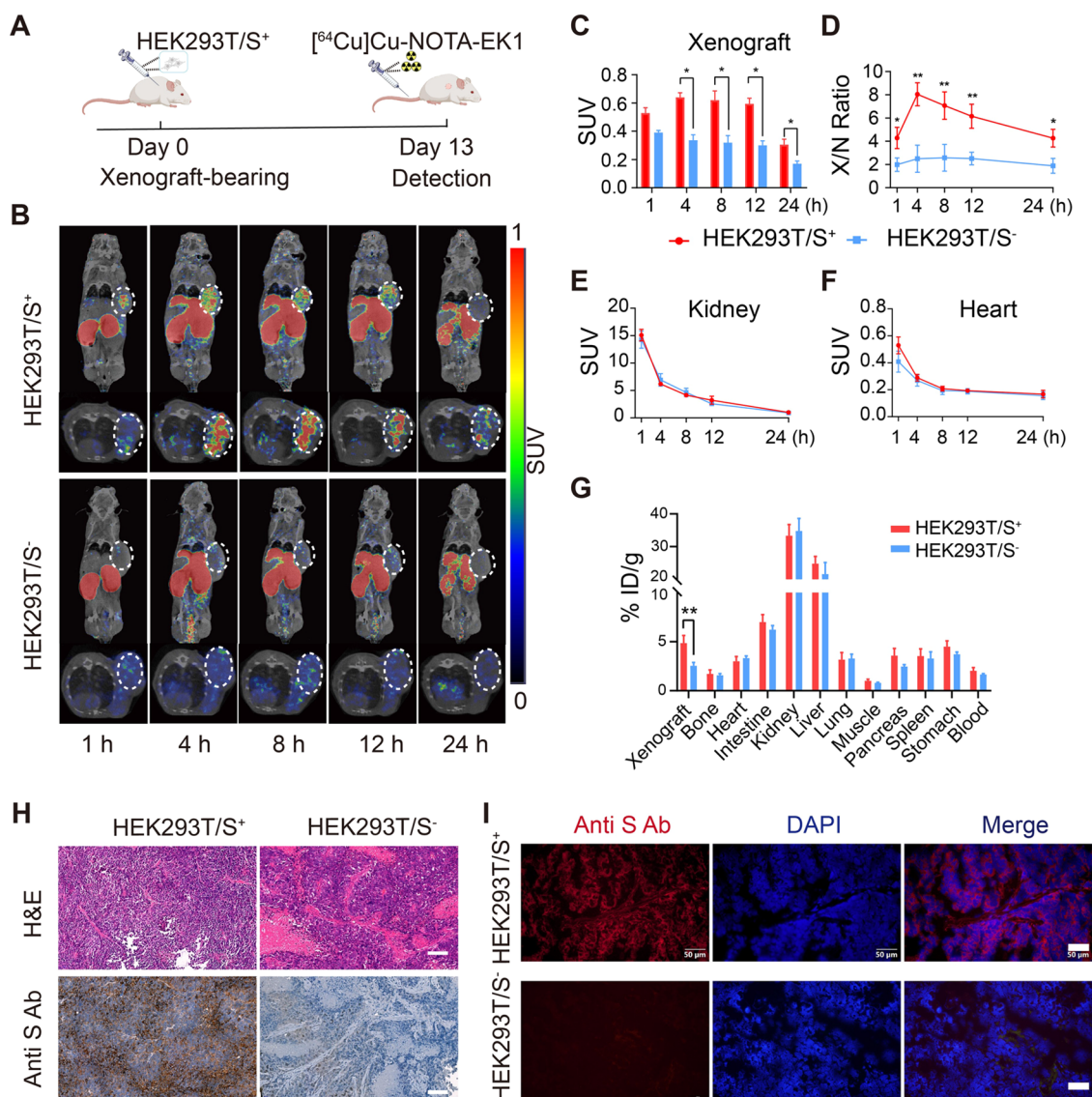
Figure 3. $[^{64}Cu]$Cu-NOTA-EK1 targeting engaged with the S-protein of SARS-CoV-2 in HEK293T/S$^+$ cell xenograft-bearing mice. (A) Flow chart for PET/CT imaging in the HEK293T/S$^+$ cell xenograft model. (B) PET/CT imaging of HEK293T/S$^+$ xenograft-bearing mice (top panel) and HEK293T/S$^-$ control mice (bottom panel). (C) Quantification of radioactivity (SUVmax) of xenografts at 1, 4, 8, 12, and 24 h p.i. of $[^{64}Cu]$Cu-NOTA-EK1. (D) Xenograft-to-normal ratios (X/N) were significantly different between HEK293T/S$^+$ and HEK293T/S$^-$ xenograft-bearing mice at each time point. (E and F) No significant difference in the time active curve (TAC) was found between the two groups in the kidney and heart. (G) *Ex vivo* biodistribution of $[^{64}Cu]$Cu-NOTA-EK1 at 24 h postinjection. (H) H&E and IHC staining for the anti-S-protein antibody for both HEK293T/S$^+$ and HEK293T/S$^-$ xenograft tissues (scale bar: 50 μm). (I) Anti-S-protein antibody (red) and DAPI (blue) from IF staining of the HEK293T/S$^+$ and HEK293T/S$^-$ xenograft (scale bar: 50 μm). Data are presented as mean ± SD, all n = 3 (*P < 0.05, **P < 0.01).

performed on xenograft sections. For IHC staining, sections were incubated with an anti-S-protein antibody (SinoBiological, Beijing, China) at 4 °C overnight, followed by the corresponding goat anti-rabbit IgG secondary antibody polymer (Jackson ImmunoResearch Laboratories, West Grove, USA) for 30 min at room temperature. After being treated with liquid 3,3-diaminobenzidine plus substrate chromogen (MXB Biotechnologies, Fuzhou, China) and counterstained with hematoxylin, the sections were scanned using a Panoramic III scanner (3DHISTECH Inc., Budapest, Hungary). Finally, each sample underwent digital image analysis performed by 3DHISTECH Quant Center software. IF staining was performed to visualize the cellular location of the S-protein. The sections were photographed under a light

microscope (Olympus Inc., Tokyo, Japan) or a confocal microscope.

2.11. Statistical Analysis. Data are expressed as mean ± standard deviation (SD). GraphPad Prism 8.0 software (GraphPad Software, La Jolla, USA) was used for statistical analysis. Comparisons between groups were performed using an unpaired two-tailed Student's t test or two-way analysis of variance (ANOVA) with Bonferroni's multiple comparisons posttest, with P < 0.05 representing a statistically significant difference.

3. RESULTS

3.1. Preparation and Characterization of $[^{64}Cu]$Cu-NOTA-EK1. EK1 is a peptide with a high conservative amino acid sequence to the S2 subunit of the S-protein in the human
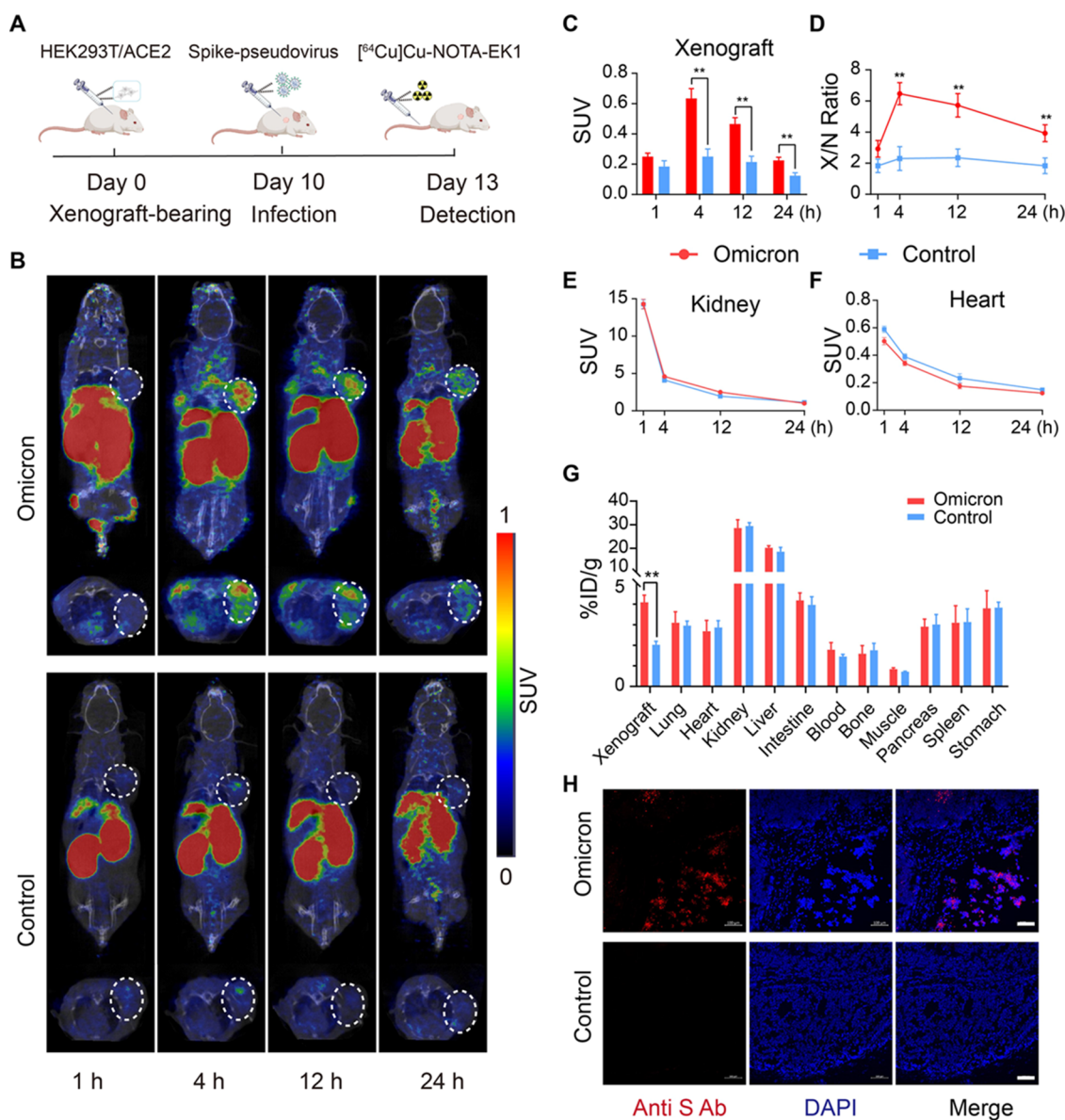
Figure 4. [^{64}Cu]Cu-NOTA-EK1 targeting engaged with the S2 subunit of SARS-CoV-2 in HEK293T/ACE2 infection xenograft-bearing mice. (A) Flow chart for PET/CT imaging in the spike-pseudotyped virus-infected HEK293T/ACE2 xenograft model. (B) PET/CT imaging of the HEK293T/ACE2 xenograft model treating with 50 μL of omicron PsV + 50 μL PBS (top panel) and 100 μL of PBS (bottom panel). (C) Quantification of radioactivity (SUVmax) of xenograft tumors and normal at 1, 4, 12, and 24 h postinjection of [^{64}Cu]Cu-NOTA-EK1. (D) Xenograft-to-normal ratios (X/N) of the HEK293T/ACE2 xenograft model among omicron and control groups at each time point ($n = 3$). (E and F) No significant difference of the TAC was found between the two groups in the kidney and heart. (G) *Ex vivo* biodistribution of [^{64}Cu]Cu-NOTA-EK1 at 24 h postinjection. (H) Representative images for the anti S-protein antibody (red) and DAPI (blue) from IF staining of the HEK293T/ACE2 xenograft model with different treatments (scale bar: 100 μm). Data are presented as mean ± SD, $n = 3$. (**$P < 0.01$).

coronavirus and the MHV-A59.[22,26,27] NOTA-EK1 were synthesized using the solid-phase peptide synthesis method and subjected to HPLC analysis, which showed that the purity of the peptide was >95% (Figure S2). To determine the safety of this probe, we performed a high-concentration dosing treatment to determine the toxicity of NOTA-EK1 (Figure S5A). After 36 h, the cells covered the entire culture plate, and no obvious inhibition of cell proliferation was observed, indicating that these peptides had no adverse effect on the cells' viability. Again, these peptides showed no significant toxicity *in vivo* (Figure S5B−D). The reaction scheme for the radiolabeling of the NOTA-EK1 peptide with ^{64}Cu is shown in Figure 2A. The radiotracer [^{64}Cu]Cu-NOTA-EK1 was successfully produced with radiochemical yields (RCY) of

more than 95% and high radiochemical purity (RCP) (>95%), as determined by radio-TLC and radio-HPLC analysis (Figure 2B). The molar activity was 10.1−15.5 GBq/μmol. The *in vitro* stability of [^{64}Cu]Cu-NOTA-EK1 was tested in sterile saline solution and human serum. Although the retention time of the tracer in serum was slightly reduced than in saline (95%, 85%, and 80% of the portion compared to the saline at 2, 12, and 24 h, respectively); overall, the radio-HPLC showed that [^{64}Cu]Cu-NOTA-EK1 was stable up to 24 h both in saline and in human serum (Figure 2C).

3.2. *In Vitro* Binding Affinity. We coated the purified protein on a 96-well microplate to test the binding potency of the tracer for the S-protein of SARS-CoV-2 using serial dilutions of the biotin-EK1 and streptavidin amplification
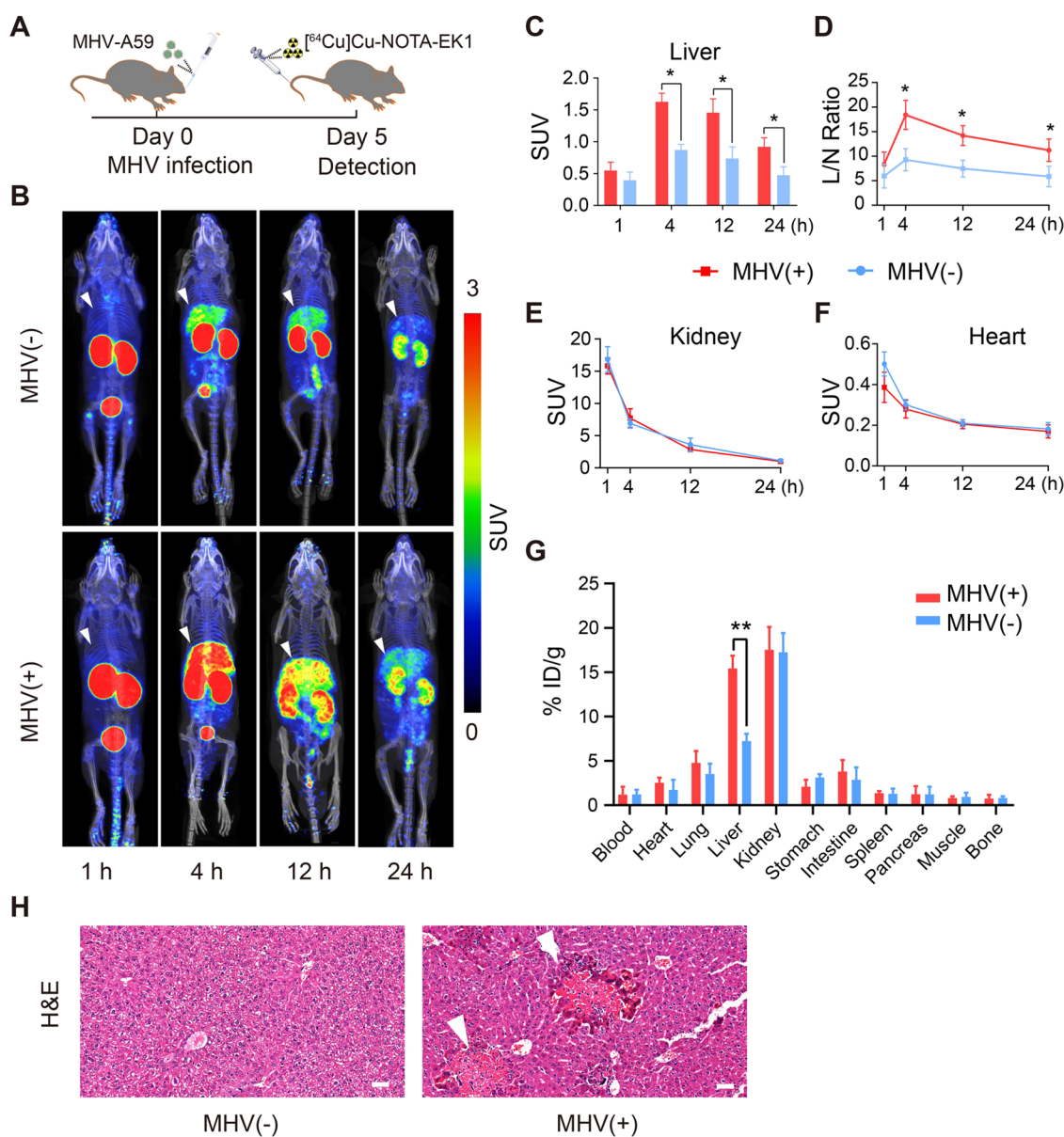
Figure 5. PET/CT imaging indicated that $[^{64}Cu]$Cu-NOTA-EK1 targeting engaged with MHV-A59 in the infection C57BL/6 mice. (A) Flow chart for PET/CT imaging in the MHV-A59 infection model. (B) Representative MIP of PET images of C57BL/6 mice intranasal injected with PBS (upper) and MHV-A59 virus (bottom). (C) Quantification of radioactivity (SUVmax) at 1, 4, 12, and 24 h postinjection of $[^{64}Cu]$Cu-NOTA-EK1, which were significantly different in the MHV-A59(−) mice model and MHV-A59(+) mice model at 4, 12, and 24 h ($n = 3$). (D) Liver-to-normal (L/N) ratios of MHV-A59(+) mice were significantly higher than the control group in 4, 12, and 24 h. (E and F) No significant difference of the TAC was found between the two groups in the kidney and heart. (G) *Ex vivo* biodistribution of $[^{64}Cu]$-NOTA-EK1 at 24 h postinjection. (H) Representative images from H&E of the liver tissue. There were plenty of lesions in the liver tissue. Data are presented as mean ± SD, $n = 3$. (*$P < 0.05$, **$P < 0.01$).

system. The saturation binding curve revealed that biotin-EK1 was able to specifically bound to the S protein. The calculated K_d of biotin-EK1 was 3.56 ± 0.38 nM ($n = 4$) (Figure. 2D). The competitive inhibition curve (IC$_{50}$ and K_i)[30] for NOTA-EK1 to biotin-EK1 was 15.02 ± 0.59 and 3.94 ± 0.51 nM ($n = 4$) (Figure 2E). The ELISA curve-fitted binding potency, including the K_d and K_i values, indicated that the newly synthesized peptide NOTA-EK1 had a nanomolar binding affinity to the S-protein. Thus, the HEK293/S$^+$ cell line was successfully established (Figure S3A, B). The results of cellular uptake of $[^{64}Cu]$Cu-NOTA-EK1 were from $2.457 \pm 0.142\%$ at 2 h to $2.570 \pm 0.154\%$ at 4 h in the HEK293T/S$^+$ cells, while it was drastically low in the HEK293T/S$^-$ cells, from $0.083 \pm$

0.015% at 2 h and $0.087 \pm 0.021\%$ at 4 h. ($P < 0.0001$, $n = 6$) (Figure 2F). The result showed that cellular uptake $[^{64}Cu]$Cu-NOTA-EK1 was increased in a S-protein of the SARS-CoV-2 dependent manner.

3.3. PET/CT Imaging of $[^{64}Cu]$Cu-NOTA-EK1 in the HEK293T/S$^+$ Xenograft-Bearing Mice Model. Whole-body PET/CT imaging was performed using SCID mice bearing HEK293T/S$^+$ and HEK293T/S$^-$ cell xenografts (Figure 3A) to visualize SARS-CoV-2 in deep tissue or organs. After intravenous injection of $[^{64}Cu]$Cu-NOTA-EK1, xenografts on the right flank were highly visible for up to 24 h (Figure 3B). The SUV of the $[^{64}Cu]$Cu-NOTA-EK1 tracer in the HEK293T/S$^+$ xenografts ($n = 3$) were 0.529 ± 0.038, 0.640

$\pm$ 0.032, 0.620 $\pm$ 0.066, 0.594 $\pm$ 0.039, and 0.305 $\pm$ 0.038 at 1, 4, 8, 12, and 24 h after intravenous injection, respectively (Figure 3C). In the HEK293T/S$^-$ xenograft group (n = 3), the SUV of the xenografts were only 0.391 $\pm$ 0.015, 0.337 $\pm$ 0.038, 0.319 $\pm$ 0.050, 0.300 $\pm$ 0.032, and 0.171 $\pm$ 0.019 at the same time points, respectively, which was significantly lower than that of HEK293T/S$^+$ xenografts at 4, 8, 12, and 24 h (P < 0.05) (Figure 3C). The xenograft-to-muscle ratio of HEK293 T/S$^+$ xenograft-bearing mice ($X/N_{S_+}^{\text{xenograft}}$ 4.28 $\pm$ 0.91, 8.04 $\pm$ 0.99, 7.07 $\pm$ 1.18, 6.15 $\pm$ 1.03, and 4.27 $\pm$ 0.76) was much higher than that of the control group ($X/N_S\_^{\text{xenograft}}$ 1.98 $\pm$ 0.58, 2.50 $\pm$ 1.17, 2.58 $\pm$ 1.15, 2.51 $\pm$ 0.55, and 1.89 $\pm$ 0.64) at 1, 4, 8, 12, and 24 h, respectively (P < 0.05) (Figure 3D). No significant difference in the TAC was found between the two groups in the kidney and heart (Figure 3E and F).

By using γ-counter, the xenografts and the major organs of xenograft-bearing mice of HEK293T/S$^+$ (n = 3) and HEK293T/S$^-$ (n = 3) were examined for the ex vivo biodistribution of [^{64}Cu]Cu-NOTA-EK1. The results were consistent with PET/CT images. The value of tracer binding of [^{64}Cu]Cu-NOTA-EK1 in the HEK293T/S$^+$ xenografts was 5.00 $\pm$ 0.83 %ID/g at 24 h postinjection, while in the HEK293T/S$^-$ xenografts, it was only 2.23 $\pm$ 0.27 %ID/g (Figure 3G). In addition, high kidney radioactivity was observed, suggesting that the renal system cleared [^{64}Cu]Cu-NOTA-EK1. Weak liver and intestinal radioactivity were also detected, implying that the liver–intestine system partially eliminated [^{64}Cu]Cu-NOTA-EK1. Other major organs, including the heart, stomach, lung, spleen, bone, muscle, and pancreas, did not exhibit significant tracer binding, indicating low background tracer binding in vivo (Figure 3G). The results of ex vivo biodistribution demonstrated that [^{64}Cu]Cu-NOTA-EK1 targeted HEK293T/S$^+$ xenografts in vivo. To further confirm that the tracer detected the S-protein in the live subjects, H&E and IHC were performed to determine the S-protein expression level in HEK293T/S$^+$ and HEK293T/S$^-$ xenograft tissues from xenograft-bearing mice injected with [^{64}Cu]Cu-NOTA-EK1 (Figure 3H). IHC analysis showed strong staining in HEK293T/S$^+$ xenograft tissues and weak staining in the control group, consistent with previous cellular tracer binding experimental studies (Figure 3H). In addition, the IF analysis of the frozen section showed the S-protein of SARS-CoV-2 in xenograft tissues (Figure 3I).

3.4. PET/CT Imaging of [^{64}Cu]Cu-NOTA-EK1 in the PsV Infection HEK293T/ACE2-Bearing Mice Model. PET/CT imaging for HEK293T/ACE2 xenograft-bearing mice infected with the omicron strain of SARS-CoV-2 PsV was performed to assess further the ability of [^{64}Cu]Cu-NOTA-EK1 to quantify the account of infectious cells (Figure 4A). The PsV infection process is shown in Figure S4A. HEK293T/ACE2 xenograft-bearing mice were infected with PsV covering the S-protein from the omicron strain (Figure S4B,C). At 72 h postinfection with the PsV, PET/CT imaging of SARS-CoV-2 PsV with intravenous injection of [^{64}Cu]Cu-NOTA-EK1 indicated drastically high signal xenograft-to-background between PsV infection xenografts and PBS injection xenografts up to 24 h (Figure 4B). The SUV values of [^{64}Cu]Cu-NOTA-EK1 in the HEK293T/ACE2 xenografts infected with omicron PsV at 1, 4, 12, and 24 h were 0.250 $\pm$ 0.023, 0.634 $\pm$ 0.065, 0.465 $\pm$ 0.042, and 0.225 $\pm$ 0.020, respectively, which were significantly higher than that of HEK293/ACE2 xenografts injected with PBS controls at 4, 12, and 24 h (n = 3, P < 0.01) (Figure 4C). Furthermore, the xenograft-to-muscle ratio of the HEK293T/

ACE2 xenograft infected with the omicron PsV ($X/N^{\text{pseudovirus}}$ 2.93 $\pm$ 0.54, 6.47 $\pm$ 0.71, 5.72 $\pm$ 0.75, and 3.92 $\pm$ 0.55) was much higher than that of the control group (X/N^{control} 1.83 $\pm$ 0.43, 2.30 $\pm$ 0.77, 2.34 $\pm$ 0.56, and 1.83 $\pm$ 0.50) at 1, 4, 12, and 24 h, respectively (P < 0.01) (Figure 4D). No significant difference in TAC was found between the two groups in the kidney and heart (Figure 4E, F).

The ex vivo biodistribution of [^{64}Cu]Cu-NOTA-EK1 in all HEK293T/ACE2 xenograft-bearing mice infected with PsV was analyzed with the γ-counter. At 24 h postinjection, the tracer binding of [^{64}Cu]Cu-NOTA-EK1 in the PsV infection was 4.092 $\pm$ 0.351 %ID/g (n = 3). These values are higher than the value of the native control, which was 2.027 $\pm$ 0.169 %ID/g (n = 3) (Figure 4G). Other major organs, such as the heart, kidney, spleen, lung, stomach, bone, muscle, and pancreas, exhibited similar tracer binding to PsV infection in vivo, indicating that [^{64}Cu]Cu-NOTA-EK1 specific selectively to SARS-CoV-2 PsV infection. In addition, we performed post-PET IF analysis further confirmed the specificity of [^{64}Cu]Cu-NOTA-EK1 (Figure 4H).

3.5. PET/CT Imaging of [^{64}Cu]Cu-NOTA-EK1 in the MHV-A59-Infected Mice. The MHV-A59, a beta-coronavirus with a highly homologous S2 subunit to the SARS-CoV-2, could be used as a surrogate virus in the biosafety level 2 (BSL-2) environment to ensure the specificity of [^{64}Cu]Cu-NOTA-EK1 for the S2 subunit in the real infection. The MHV-A59-infected C57BL/6 J mice had higher levels of radioactive accumulation in their livers after injection at 4, 12, and 24 h compared to the control group (Figure 5A, B). In addition, the values of SUV in the liver and liver-to-muscle signal (L/N) ratios were significantly higher than those in the control group at 4, 12, and 24 h (Figure 5C, D). However, no significant difference in TAC was found between the two groups in the kidney and heart (Figure 5E, F).

The ex vivo biodistribution of [^{64}Cu]Cu-NOTA-EK1 in the major organs of MHV-A59-infected mice (n = 3) was also carried out by the γ-counter. The results were consistent with PET/CT images. The high tracer binding of [^{64}Cu]Cu-NOTA-EK1 in the livers of MHV-A59-infected mice was 15.41 $\pm$ 1.44 %ID/g (2.1-fold) 24 h postinjection, while it was only 7.22 $\pm$ 0.82 %ID/g in the control group (Figure 5G). Other major organs exhibited similar tracer binding to native control in vivo, indicating that [^{64}Cu]Cu-NOTA-EK1 selectively bound to the S2 subunit from MHV-A59 in the infection model in vivo. Furthermore, infectious lesions were shown in post-PET H&E staining of liver tissues (Figure 5H). Thus, our results suggest that the [^{64}Cu]Cu-NOTA-EK1 detected the coronavirus with a conserved S2 subunit from subsequent viral infection.

4. DISCUSSION

COVID-19 is characterized by an infection in the upper and lower respiratory tracts, which can progress to life-threatening pneumonia. SARS-CoV-2 infection, however, is not restricted to the respiratory system.[10] Currently, extrapulmonary infection is barely detectable through regular nucleic acid tests. There is an urgent need to develop sensitive and effective detection methods for SARS-CoV-2 and its variants in extrapulmonary tissues. One promising method of detecting the spatiotemporal distribution of SARS-CoV-2 infection is noninvasion PET/CT agents targeting the S-protein of SARS-CoV-2.[31] EK1, a peptide-based pan-coronavirus fusion inhibitor, has been shown in previous studies to reduce

SARS-CoV-2 infection significantly by specifically targeting the spike protein.[22,27] In this study, we reported that the [64Cu]Cu-NOTA-EK1 tracer that targets the SARS-CoV-2 S-protein's conserved S2 subunit, constructed the PsV of the SARS-CoV-2 omicron strain to infect HEK293/ACE2 cells *in vivo*, and mimic the process of extrapulmonary infection in C57BL/6 J mice by MHV-A59, a kind of coronavirus where the S2 subunit is very conserved and is highly homologous to SARS-CoV-2.[25] The molecular probe [64Cu]Cu-NOTA-EK1 exhibited good biosafety and efficacy when used to target the S2 subunit of the S-protein (Figures 2−5 and S5).

Animal models are essential to carrying out these experiments because they can provide reliable and detailed tissue information that is otherwise difficult or impossible to obtain in humans. A previous study described a 64Cu-labeled CR3022-F(ab′)2 probe based on the anti-SARS-CoV-2S-protein antibody CR3022 to study the dynamics of infection within the respiratory tract and uncover novel sites of infection in rhesus macaques.[31] A strong signal was observed in extrapulmonary organoids, such as the penis, testes, prostate, and pampiniform plexus. In addition, SARS-CoV-2 virus particles and essential structures have been found in several organs, such as the appendix, eyes, heart, and brain.[32] Survivors of SARS-CoV-2 infection also exhibit an increased risk of post-acute sequelae in the pulmonary and several extrapulmonary organ systems, including cardiovascular, neurological, gastro-intestinal, and musculoskeletal disorders.[33] Whether these symptoms are caused by direct viral infection or the body's response to the virus remains unclear. As Qiao et al. point out, SARS-CoV-2 infection induces inflammatory bone loss in golden Syrian hamsters by disturbing the microenvironment in the musculoskeletal system without direct infection.[34] To better understand the pathogenesis of viral variants, we believe that animal models will continue to make a significant contribution. In addition, PET is more sensitive and less invasive when detecting viruses than antigen or nucleic acid detection in extrapulmonary lesions. Thus, we constructed a rapid and low-cost mice model for studying infection dynamics in BSL-2 laboratories in this study. PsV of SARS-CoV-2 infected mice model and MHV-infected mice model were used to verify the ability of [64Cu]Cu-NOTA-EK1 to detect the virus structure in extrapulmonary lesions. These PET imaging results suggest that [64Cu]Cu-NOTA-EK1 is effectively bound to the S2-subunit of SARS-CoV-2 VOC or MHV-A59 and produces a significant signal in infected mice models. Our study provides promising evidence that PET tracer, [64Cu]Cu-NOTA-EK1, can be used for investigating the disease pathogenesis of viral variants in extrapulmonary lesions in animal models.

The most severe SARS-CoV-2 infections result in acute respiratory distress syndrome (ARDS), and several methods are being used to diagnose ARDS and other pulmonary infections. These methods include RT-PCR, arterial blood gas analysis, high resolution computed tomography, and bedside digital radiography. Importantly, these methods are very effective and easy to use, as PET screening is not required. However, previous studies have reported long-term lung complications in patients infected with SARS-CoV and Middle East respiratory syndrome coronavirus (MERS-CoV).[35,36] Pulmonary fibrosis may be a long-term complication of coronavirus-infected patients, which increases the risk for the development of lung cancer.[37] Increasing risk of long-term pulmonary complications was also observed in survivors of

SARS-CoV-2 infection. However, methods for directly detecting latent virion in pulmonary tissue are very few. The most common method is a biopsy, which is invasive, subject to sampling bias, and leads to false negatives. Therefore, a safe, noninvasive, and sensitive method is urgently needed to detect latent virion in lungs, monitor recovering COVID-19 patients, and investigate the relevance of latent virion or its structure with pulmonary complications. In this study, we constructed SARS-CoV-2 PsV carrying an S2 subunit to investigate the efficiency of tracer bound to the S-protein from the SARS-CoV-2 omicron variant. S-protein density in infected tissues is expected to be much lower than that in control xenografts (Figures 3 and 4). Our results indicate that [64Cu]Cu-NOTA-EK1 has the potential ability to track the low-density S-protein in infected tissues and would be beneficial to studying the SARS-CoV-2 infection pathway and mechanism. Under-standing the SARS-CoV-2 infection pathway and mechanism in pulmonary organoids has significant therapeutic implica-tions.

The SARS-CoV-2 preferentially infects the proximal airway epithelium and the distal alveolar tissue in the pulmonary system, then spreads to the extrapulmonary organoids. Since the SARS-CoV-2 pandemic, there has been a dramatic increase in knowledge about liver disease caused by the coronavirus infection. Several studies have reported the detection of coronavirus particles or virus nucleic acid in liver tissues.[38,39] COVID-19 patients with liver injury or liver-related dysfunction have a higher risk of death. Furthermore, infection with SARS-CoV-2 has been linked to an inflammatory state, which may contribute to liver abnormalities that have been observed.[7] Liver abnormalities harm the patient's prognosis. However, the amount of hepatology-related knowledge on COVID-19 is limited. It is worth noting that [64Cu]Cu-NOTA-EK1 can recognize MHV-A59 (It can be used as an alternative model for studying SARS-CoV before SARS-CoV-2 comes out.[40]) in the liver as a broad-spectrum coronavirus probe. Whole-body PET/CT imaging revealed that [64Cu]Cu-NOTA-EK1 could effectively detect the virus in extra-pulmonary lesions of the MHV-A59-infected mice (Figure 5). The findings of this study suggest that one such application of this tracer is paving the way for the successful development of the coronavirus pathophysiology.

Our study has some limitations. The SARS-CoV-2 PsV are employed to imitate virus infection under BSL-2 conditions. Although we constructed a PsV system to express the S2 subunit in infectious cells, PsV could not accurately simulate the SARS-CoV-2 infection due to a single cycle of PsV infection failing to cause virus dissemination and extrapulmo-nary infection. Previous research has shown that a 64Cu-labeled probe could target spike proteins in the respiratory tract and extrapulmonary organs (penis, prostate, testis, and pampini-form plexus) of SARS-CoV-2-infected rhesus macaques.[31] In the present study, MHV-A59 serves as a surrogate for investigating the ability of the probe to detect the spike protein in extrapulmonary organ infection. Above all, the 64Cu-labeled probe could be utilized for whole-body imaging. However, there is still some room to improve the probe. For example, the probe structure could be modified to streamline the process or attach more cross-linkers to carry more 64Cu for enhancing the PET signal.[41] The potential for whole-body imaging of [64Cu]Cu-NOTA-EK1 must be tested in appropriate COVID-19 patients to verify its clinical effective-ness.

5. CONCLUSIONS

In the present study, a pan-coronavirus S-protein binding peptide, EK1, was selected and modified as a PET imaging agent [^{64}Cu]Cu-NOTA-EK1. Preclinical PET/CT imaging proved that [^{64}Cu]Cu-NOTA-EK1 specifically targeted the SARS-CoV-2 S-protein's conserved S2 subunit in the HEK293T/S-protein+ cells xenograft model, in the S-protein-pseudotyped virus-infected HEK293T/ACE2 model, and in the extrapulmonary infection by MHV-A59, beta-coronavirus a surrogate virus in the biosafety level 2 (BSL-2) environment. The molecular probe [^{64}Cu]Cu-NOTA-EK1 exhibited good biosafety and efficacy detecting the spatiotemporal distribution of SARS-CoV-2 infection and potential for molecular imaging of COVID-19 in living subjects.

■ ASSOCIATED CONTENT

ⓈI Supporting Information

The Supporting Information is available free of charge at https://pubs.acs.org/doi/10.1021/acs.molpharmaceut.2c00584.

> Chemical structure of NOTA-EK1 and the labeling process of [^{64}Cu]Cu-NOTA-EK1; quality control for NOTA-EK1; characterization of constructed HEK293T/S$^+$ and HEK293T/ACE2 cell lines; infectivity potential of omicron spike bearing SARS-CoV-2 PsVs in the HEK293T/ACE2 xenograft model; and safety assessment of NOTA-EK1 (PDF)

■ AUTHOR INFORMATION

Corresponding Authors

Hong Shan − *Guangdong Provincial Key Laboratory of Biomedical Imaging, The Fifth Affiliated Hospital and Department of Interventional Medicine, The Fifth Affiliated Hospital, Sun Yat-sen University, Zhuhai, Guangdong Province 519000, China;* ⓞ orcid.org/0000-0001-6640-1390; Email: shanhong@mail.sysu.edu.cn

Hongjun Jin − *Guangdong Provincial Key Laboratory of Biomedical Imaging, The Fifth Affiliated Hospital, Sun Yat-sen University, Zhuhai, Guangdong Province 519000, China;* ⓞ orcid.org/0000-0002-1522-1098; Phone: +86-0756-252-6136; Email: jinhj3@mail.sysu.edu.cn

Authors

Jianzhong Xian − *Guangdong Provincial Key Laboratory of Biomedical Imaging, The Fifth Affiliated Hospital and Department of Ultrasound Medicine, The Fifth Affiliated Hospital, Sun Yat-sen University, Zhuhai, Guangdong Province 519000, China*

Hongbin Huang − *Guangdong Provincial Key Laboratory of Biomedical Imaging, The Fifth Affiliated Hospital, Sun Yat-sen University, Zhuhai, Guangdong Province 519000, China*

Guolong Huang − *Guangdong Provincial Key Laboratory of Biomedical Imaging, The Fifth Affiliated Hospital, Sun Yat-sen University, Zhuhai, Guangdong Province 519000, China*

Renwei Zhou − *Guangdong Provincial Key Laboratory of Biomedical Imaging, The Fifth Affiliated Hospital, Sun Yat-sen University, Zhuhai, Guangdong Province 519000, China*

Min Yang − *Guangdong Provincial Key Laboratory of Biomedical Imaging, The Fifth Affiliated Hospital, Sun Yat-sen University, Zhuhai, Guangdong Province 519000, China*

Yifan Qiu − *Guangdong Provincial Key Laboratory of Biomedical Imaging, The Fifth Affiliated Hospital, Sun Yat-sen University, Zhuhai, Guangdong Province 519000, China*

Lei Bi − *Guangdong Provincial Key Laboratory of Biomedical Imaging, The Fifth Affiliated Hospital, Sun Yat-sen University, Zhuhai, Guangdong Province 519000, China*

Zhongzhen Su − *Guangdong Provincial Key Laboratory of Biomedical Imaging, The Fifth Affiliated Hospital and Department of Ultrasound Medicine, The Fifth Affiliated Hospital, Sun Yat-sen University, Zhuhai, Guangdong Province 519000, China*

Fei Xiao − *Guangdong Provincial Key Laboratory of Biomedical Imaging, The Fifth Affiliated Hospital, Sun Yat-sen University, Zhuhai, Guangdong Province 519000, China*

Complete contact information is available at:
https://pubs.acs.org/10.1021/acs.molpharmaceut.2c00584

Author Contributions

ǁJ.X. and H.H. contributed equally.

Notes

The authors declare the following competing financial interest(s): Patent-pending to the State Intellectual Property Office of the People's Republic of China: CN113004376A (20210106796.9), Molecular Probes for Imaging Coronavirus Infected Living Subjects and Preparation Method Thereof.

■ ACKNOWLEDGMENTS

■ REFERENCES

(1) Thakur, S.; Sasi, S.; Pillai, S. G.; Nag, A.; Shukla, D.; Singhal, R.; Phalke, S.; Velu, G. S. K. SARS-CoV-2 Mutations and their impact on diagnostics, therapeutics and vaccines. *Front. Med.* **2022**, *9*, No. 815389.

(2) Acter, T.; Uddin, N.; Das, J.; Akhter, A.; Choudhury, T. R.; Kim, S. Evolution of severe acute respiratory syndrome coronavirus 2 (SARS-CoV-2) as coronavirus disease 2019 (COVID-19) pandemic: A global health emergency. *Sci. Total Environ.* **2020**, *730*, No. 138996.

(3) Xiao, F.; Tang, M.; Zheng, X.; Liu, Y.; Li, X.; Shan, H. Evidence for gastrointestinal infection of SARS-CoV-2. *Gastroenterology* **2020**, *158*, 1831−1833.e3.

(4) Shi, S.; Qin, M.; Shen, B.; Cai, Y.; Liu, T.; Yang, F.; Gong, W.; Liu, X.; Liang, J.; Zhao, Q.; Huang, H.; Yang, B.; Huang, C. Association of cardiac injury with mortality in hospitalized patients with COVID-19 in Wuhan, China. *JAMA Cardiol.* **2020**, *5*, 802−810.

(5) Liu, Y.; Xia, P.; Cao, W.; Liu, Z.; Ma, J.; Zheng, K.; Chen, L.; Li, X.; Qin, Y.; Li, X. Divergence between serum creatine and cystatin C in estimating glomerular filtration rate of critically ill COVID-19 patients. *Renal Failure* **2021**, *43*, 1104−1114.

(6) Wu, P.; Duan, F.; Luo, C.; Liu, Q.; Qu, X.; Liang, L.; Wu, K. Characteristics of ocular findings of patients with Coronavirus Disease 2019 (COVID-19) in Hubei Province, China. *JAMA Ophthalmol.* **2020**, *138*, 575−578.

(7) Dufour, J.-F.; Marjot, T.; Becchetti, C.; Tilg, H. COVID-19 and liver disease. *Gut* **2022**, No. gutjnl-2021-326792.

(8) Mao, L.; Jin, H.; Wang, M.; Hu, Y.; Chen, S.; He, Q.; Chang, J.; Hong, C.; Zhou, Y.; Wang, D.; Miao, X.; Li, Y.; Hu, B. Neurologic manifestations of hospitalized patients with coronavirus disease 2019 in Wuhan, China. *JAMA Neurol.* **2020**, *77*, 683−690.

(9) Ning, Q.; Wu, D.; Wang, X.; Xi, D.; Chen, T.; Chen, G.; Wang, H.; Lu, H.; Wang, M.; Zhu, L.; Hu, J.; Liu, T.; Ma, K.; Han, M.; Luo, X. The mechanism underlying extrapulmonary complications of the coronavirus disease 2019 and its therapeutic implication. *Signal Transduction Targeted Ther.* **2022**, *7*, 57.

(10) Lamers, M. M.; Haagmans, B. L. SARS-CoV-2 pathogenesis. *Nat. Rev. Microbiol.* **2022**, *20*, 270−284.

(11) Chung, M.; Bernheim, A.; Mei, X.; Zhang, N.; Huang, M.; Zeng, X.; Cui, J.; Xu, W.; Yang, Y.; Fayad, Z. A.; Jacobi, A.; Li, K.; Li, S.; Shan, H. CT imaging features of 2019 novel coronavirus (2019-nCoV). *Radiology* **2020**, *295*, 202−207.

(12) Lu, W.; Zhang, S.; Chen, B.; Chen, J.; Xian, J.; Lin, Y.; Shan, H.; Su, Z. Z. A clinical study of noninvasive assessment of lung lesions in patients with coronavirus disease-19 (COVID-19) by bedside ultrasound. *Ultraschall Med.* **2020**, *41*, 300−307.

(13) Xian, J.; Pei, X.; Lu, W.; Zhong, H.; Lin, Y.; Jin, H.; Su, Z. The clinical value of bedside ultrasound in predicting the severity of coronavirus disease-19 (COVID-19). *Ann. Transl. Med.* **2021**, *9*, 336.

(14) Jain, S. K. The promise of molecular imaging in the study and treatment of infectious diseases. *Mol. Imaging Biol.* **2017**, *19*, 341−347.

(15) Gambhir, S. S. Molecular imaging of cancer with positron emission tomography. *Nat. Rev. Cancer* **2002**, *2*, 683−693.

(16) Minamimoto, R.; Hotta, M.; Ishikane, M.; Inagaki, T. FDG-PET/CT images of COVID-19: a comprehensive review. *Global Health Med.* **2020**, *2*, 221−226.

(17) Yao, J.; Liu, J.; Bi, L.; Zhang, F.; Huang, Y.; Shan, H.; Wang, Y.; Jin, H. Quantitative dynamic ^{18}F-FDG-PET/CT imaging revealed residual lesions in discharged COVID-19 patients. *J. Nucl. Med.* **2021**, *62*, 185−185.

(18) Zhu, H.; Zhang, H.; Zhou, N.; Ding, J.; Jiang, J.; Liu, T.; Liu, Z.; Wang, F.; Zhang, Q.; Zhang, Z.; Yan, S.; Li, L.; Benabdallah, N.; Jin, H.; Liu, Z.; Cai, L.; Thorek, D. L. J.; Yang, X.; Yang, Z. Molecular PET/CT profiling of ACE2 expression in vivo: implications for infection and outcome from SARS-CoV-2. *Adv. Sci.* **2021**, *8*, No. e2100965.

(19) Ruiz-Bedoya, C. A.; Mota, F.; Ordonez, A. A.; Foss, C. A.; Singh, A. K.; Praharaj, M.; Mahmud, F. J.; Ghayoor, A.; Flavahan, K.; De Jesus, P.; Bahr, M.; Dhakal, S.; Zhou, R.; Solis, C. V.; Mulka, K. R.; Bishai, W. R.; Pekosz, A.; Mankowski, J. L.; Villano, J.; Klein, S. L.; Jain, S. K. ^{124}I-Iodo-DPA-713 positron emission tomography in a hamster model of SARS-CoV-2 infection. *Mol. Imaging Biol.* **2022**, *24*, 135−143.

(20) Yan, R.; Zhang, Y.; Li, Y.; Xia, L.; Guo, Y.; Zhou, Q. Structural basis for the recognition of SARS-CoV-2 by full-length human ACE2. *Science* **2020**, *367*, 1444−1448.

(21) Wang, Q.; Zhang, Y.; Wu, L.; Niu, S.; Song, C.; Zhang, Z.; Lu, G.; Qiao, C.; Hu, Y.; Yuen, K. Y.; Wang, Q.; Zhou, H.; Yan, J.; Qi, J. Structural and functional basis of SARS-CoV-2 entry by using human ACE2. *Cell* **2020**, *181*, 894.e9−904.e9.

(22) Xia, S.; Liu, M.; Wang, C.; Xu, W.; Lan, Q.; Feng, S.; Qi, F.; Bao, L.; Du, L.; Liu, S.; Qin, C.; Sun, F.; Shi, Z.; Zhu, Y.; Jiang, S.; Lu, L. Inhibition of SARS-CoV-2 (previously 2019-nCoV) infection by a highly potent pan-coronavirus fusion inhibitor targeting its spike protein that harbors a high capacity to mediate membrane fusion. *Cell Res.* **2020**, *30*, 343−355.

(23) Xia, S.; Zhu, Y.; Liu, M.; Lan, Q.; Xu, W.; Wu, Y.; Ying, T.; Liu, S.; Shi, Z.; Jiang, S.; Lu, L. Fusion mechanism of 2019-nCoV and fusion inhibitors targeting HR1 domain in spike protein. *Cell. Mol. Immunol.* **2020**, *17*, 765−767.

(24) Tharappel, A. M.; Samrat, S. K.; Li, Z.; Li, H. Targeting crucial host factors of SARS-CoV-2. *ACS Infect. Dis.* **2020**, *6*, 2844−2865.

(25) Cai, Y.; Zhang, J.; Xiao, T.; Peng, H.; Sterling, S. M.; Walsh, R. M., Jr.; Rawson, S.; Rits-Volloch, S.; Chen, B. Distinct conformational states of SARS-CoV-2 spike protein. *Science* **2020**, *369*, 1586−1592.

(26) Wang, X.; Xia, S.; Zhu, Y.; Lu, L.; Jiang, S. Pan-coronavirus fusion inhibitors as the hope for today and tomorrow. *Protein Cell* **2021**, *12*, 84−88.

(27) Xia, S.; Yan, L.; Xu, W.; Agrawal, A. S.; Algaissi, A.; Tseng, C. K.; Wang, Q.; Du, L.; Tan, W.; Wilson, I. A.; Jiang, S.; Yang, B.; Lu, L. A pan-coronavirus fusion inhibitor targeting the HR1 domain of human coronavirus spike. *Sci. Adv.* **2019**, *5*, No. eaav4580.

(28) Peng, T.; Wang, X.; Li, Z.; Bi, L.; Gao, J.; Yang, M.; Wang, Y.; Yao, X.; Shan, H.; Jin, H. Preclinical evaluation of [^{64}Cu]NOTA-CP01 as a PET imaging agent for metastatic esophageal squamous cell carcinoma. *Mol. Pharmaceutics* **2021**, *18*, 3638−3648.

(29) Li, B.; Wang, W.; Song, W.; Zhao, Z.; Tan, Q.; Zhao, Z.; Tang, L.; Zhu, T.; Yin, J.; Bai, J.; Dong, X.; Tan, S.; Hu, Q.; Tang, B. Z.; Huang, X. Antiviral and anti-inflammatory treatment with multifunctional alveolar macrophage-like nanoparticles in a surrogate mouse model of COVID-19. *Adv. Sci.* **2021**, *8*, No. 2003556.

(30) Cer, R. Z.; Mudunuri, U.; Stephens, R.; Lebeda, F. J. IC50-to-Ki: a web-based tool for converting IC50 to Ki values for inhibitors of enzyme activity and ligand binding. *Nucleic Acids Res.* **2009**, *37*, W441−W445.

(31) Madden, P.; Thomas, Y.; Blair, R.; Samer, S.; Doyle, M.; Midkiff, C.; Doyle-Meyers, L.; Becker, M.; Arif, S.; McRaven, M.; Simons, L.; Carias, A.; Martinelli, E.; Lorenzo-Redondo, R.; Hultquist, J.; Villinger, F.; Veazey, R.; Hope, T. An immunoPET probe to SARS-CoV-2 reveals early infection of the male genital tract in rhesus macaques. *bioRxiv* **2022**, No. 481974.

(32) Stokel-Walker, C. How long does SARS-CoV-2 stay in the body? *BMJ* **2022**, *377*, No. o1555.

(33) Al-Aly, Z.; Bowe, B.; Xie, Y. Long COVID after breakthrough SARS-CoV-2 infection. *Nat. Med.* **2022**, *28*, 1461−1467.

(34) Qiao, W.; Lau, H. E.; Xie, H.; Poon, V. K.; Chan, C. C.; Chu, H.; Yuan, S.; Yuen, T. T.; Chik, K. K.; Tsang, J. O.; Chan, C. C.; Cai, J. P.; Luo, C.; Yuen, K. Y.; Cheung, K. M.; Chan, J. F.; Yeung, K. W. SARS-CoV-2 infection induces inflammatory bone loss in golden Syrian hamsters. *Nat. Commun.* **2022**, *13*, 2539.

(35) Zhang, P.; Li, J.; Liu, H.; Han, N.; Ju, J.; Kou, Y.; Chen, L.; Jiang, M.; Pan, F.; Zheng, Y.; Gao, Z.; Jiang, B. Long-term bone and lung consequences associated with hospital-acquired severe acute respiratory syndrome: a 15-year follow-up from a prospective cohort study. *Bone Res.* **2020**, *8*, 8.

(36) Das, K. M.; Lee, E. Y.; Singh, R.; Enani, M. A.; Al Dossari, K.; Van Gorkom, K.; Larsson, S. G.; Langer, R. D. Follow-up chest radiographic findings in patients with MERS-CoV after recovery. *Indian J. Radiol. Imaging* **2017**, *27*, 342−349.

(37) Khiali, S.; Rezagholizadeh, A.; Entezari-Maleki, T. SARS-CoV-2 and probable lung cancer risk. *BioImpacts* **2022**, *12*, 291−292.

(38) Chornenkyy, Y.; Mejia-Bautista, M.; Brucal, M.; Blanke, T.; Dittmann, D.; Yeldandi, A.; Boike, J. R.; Lomasney, J. W.; Nayar, R.; Jennings, L. J.; Pezhouh, M. K. Liver pathology and SARS-CoV-2 detection in formalin-fixed tissue of patients with COVID-19. *Am. J. Clin. Pathol.* **2021**, *155*, 802−814.

(39) Kaltschmidt, B.; Fitzek, A. D. E.; Schaedler, J.; Förster, C.; Kaltschmidt, C.; Hansen, T.; Steinfurth, F.; Windmöller, B. A.; Pilger, C.; Kong, C.; Singh, K.; Nierhaus, A.; Wichmann, D.; Sperhake, J.; Püschel, K.; Huser, T.; Krüger, M.; Robson, S. C.; Wilkens, L.; Esch, S. A. J. Hepatic vasculopathy and regenerative responses of the liver in fatal cases of COVID-19. *Clin. Gastroenterol. Hepatol.* **2021**, *19*, 1726.e3−1729.e3.

(40) Yang, Z.; Du, J.; Chen, G.; Zhao, J.; Yang, X.; Su, L.; Cheng, G.; Tang, H. Coronavirus MHV-A59 infects the lung and causes severe pneumonia in C57BL/6 mice. *Virol. Sin.* **2014**, *29*, 393−402.

(41) Seo, J. W.; Ingham, E. S.; Mahakian, L.; Tumbale, S.; Wu, B.; Aghevlian, S.; Shams, S.; Baikoghli, M.; Jain, P.; Ding, X.; Goeden, N.; Dobreva, T.; Flytzanis, N. C.; Chavez, M.; Singhal, K.; Leib, R.; James, M. L.; Segal, D. J.; Cheng, R. H.; Silva, E. A.; Gradinaru, V.; Ferrara, K. W. Positron emission tomography imaging of novel AAV capsids maps rapid brain accumulation. *Nat. Commun.* **2020**, *11*, 2102.